Chemical Science

ROYAL SOCIETY OF CHEMISTRY

EDGE ARTICLE

View Article Online
View Journal | View Issue

Cite this: *Chem. Sci.*, 2020, **11**, 9593

All publication charges for this article have been paid for by the Royal Society of Chemistry

A conductive metal–organic framework photoanode†

Brian Pattengale, *[a] Jessica G. Freeze, [a] Matthew J. Guberman-Pfeffer, [b] Ryotaro Okabe,‡[b] Sarah Ostresh, [a] Subhajyoti Chaudhuri, [a] Victor S. Batista *[a] and Charles A. Schmuttenmaer §[a]

We report the development of photosensitizing arrays based on conductive metal–organic frameworks (MOFs) that enable light harvesting and efficient charge separation. Zn_2TTFTB (TTFTB = tetrathiafulvalene tetrabenzoate) MOFs are deposited directly onto TiO_2 photoanodes and structurally characterized by pXRD and EXAFS measurements. Photoinduced interfacial charge transfer dynamics are investigated by combining time-resolved THz spectroscopy and quantum dynamics simulations. Sub-600 fs electron injection into TiO_2 is observed for Zn_2TTFTB–TiO_2 and is compared to the corresponding dynamics for TTFTB–TiO_2 analogues that lack the extended MOF architecture. Rapid electron injection from the MOF into TiO_2 is enhanced by facile migration of the hole away from the interfacial region. Holes migrate through strongly coupled HOMO orbitals localized on the tetrathiafulvalene cores of the columnar stacks of the MOF, whereas electrons are less easily transferred through the spiral staircase arrangement of phenyl substituents of the MOF. The reported findings suggest that conductive MOFs could be exploited as novel photosensitizing arrays in applications to slow, and thereby make difficult, photocatalytic reactions such as those required for water-splitting in artificial photosynthesis.

Received 5th August 2020
Accepted 14th August 2020

DOI: 10.1039/d0sc04302h

rsc.li/chemical-science

Introduction

Photocatalytic reactions, including those required for artificial photosynthesis, are initiated by photoinduced charge separation.[1–8] Interfacial charge transfer at the electrode surface allows separation of the photogenerated electron–hole pair, transferring the electron (or, the hole) across the interface.[9–16] The charge-separation process has been extensively studied in photoanodes of dye-sensitized photoelectrochemical cells[17–20] where photoexcited molecular dyes inject electrons into the conduction band of a metal oxide, leaving electron–holes on the dyes anchored to the electrode surface. The holes are then transferred to an oxidation catalyst to perform, for example, water oxidation.[21–25] A critical challenge with such systems, however, is electron–hole recombination (*e.g.*, recombination of electrons from the conduction band of the metal oxide with holes localized on the surface chromophore, as in dye-sensitized solar cells (DSSCs)).[26–30] Therefore, it is important to design architectures that extend the lifetime of charge-separated states and enable slow, multielectron photocatalytic reactions.

Passivation of the metal-oxide surface with a blocking layer is a common technique applied to suppress recombination of electrons in the conduction band with redox species in the electrolyte.[26,28–31] Another strategy is to focus on the localization of the hole within the photosensitizer component of the system. For example, recombination dynamics have been altered in molecular photosensitizers by modifying the anchoring group,[32,33] the linker conjugation,[34] or the linker length.[35] However, such systems can be difficult to synthesize and tune, especially when an additional level of complexity is added by the requirement of interfacing the photosensitizer with a catalyst to perform useful redox reactions. Here, we focus on using a photosensitizer based on heterogeneous materials that can be highly tunable and easily functionalized to enable efficient separation of the hole from the metal-oxide surface, and transfer to an oxidation catalyst. Similar strategies has been used in various classes of heterogeneous materials.[36–38] We focus on microporous materials that can be designed to have visible light absorption and suitable conductivity, namely conductive metal–organic frameworks.[39–42]

MOFs have an extensive track-record of utility in heterogeneous catalysis, either as intrinsically catalytic or by

[a]*Department of Chemistry and Yale Energy Sciences Institute, Yale University, New Haven, Connecticut 06520-8107, USA. E-mail: brian.pattengale@yale.edu; victor.batista@yale.edu*

[b]*Department of Molecular Biophysics and Biochemistry, Yale Microbial Sciences Institute, Yale University, New Haven, Connecticut 06520-8107, USA*

† Electronic supplementary information (ESI) available: Experimental methods and details, supplementary figures for characterization, spectroelectrochemistry, OPTP, and computational results including optimized coordinates for the utilized models. See DOI: 10.1039/d0sc04302h

‡ Present address: School of Life Science and Technology, Tokyo Institute of Technology, Nagatsuta 4259, Midori-ku, Yokohama, Kanaga-wa 226-8503, Japan.

§ Deceased July 26, 2020.

functionalization to incorporate catalysts.[43–53] Conductive MOFs often have spatially overlapping ligands that form continuous electronic bands and mediate through-space charge transfer.[39,40,42,54] In such systems, the overlapping ligands form a photosensitizing array that allows charge carrier migration along crystallographically-oriented chromophores. Such a design enables holes to migrate away from the metal oxide surface, or alternatively allow electrons to migrate to the surface for interfacial charge transfer. Therefore, conductive MOFs are attractive photosensitizing arrays for enabling charge separation as necessary to perform slow multielectron catalytic transformations. Such a design is reminiscent of light-harvesting and photocatalysis in natural photosynthesis, where the slow multielectron water oxidation reaction is enabled by photosensitizing chromophore units, such as P680 and pheophytin, that transfer electrons through quinone redox co-factors to separate electron–hole pairs over long distances, and inhibit charge recombination.[55] Notably, related MOF systems relying on energy transfer mechanisms have been developed and applied to solar energy technologies,[56–58] however their conductive counterparts relying on charge transfer have been much less investigated.[59,60]

In this work, we utilize a conductive MOF that functions as a visible-light photosensitizing array when deposited on TiO_2. Optical-pump THz-probe spectroscopy (OPTP) shows that the Zn_2TTFTB conductive MOF injects electrons into the conduction band of TiO_2. Computational modelling provides understanding of the charge transport mechanism in Zn_2TTFTB–TiO_2. Nanosecond transient absorption spectroscopy (ns-TA) shows that the lifetime of the electron–hole pair is significantly increased in the MOF-sensitized system, when compared to TiO_2 sensitized only with the ligand. Therefore, the conductive MOF array is essential for electron–hole pair separation, yielding photoanodes that might be particularly suitable to perform slow and, thereby, difficult photocatalytic oxidation reactions.

Results and discussion

Zn_2TTFTB structural characterization

The Zn_2TTFTB MOF was chosen for development of photosensitizing arrays due to its visible light absorption, stability under irradiation, and sub-picosecond photoconductivity dynamics.[42,54,61] It was synthesized using tetrathiafulvalene tetrabenzoate (TTFTB) and Zn^{2+} and computationally characterized by using model systems of varying complexity, including a half-unit cell of the MOF structure consisting of a columnar stack of TTFTB ligands (denoted as the 3-layer model; Fig. 1a and b), a single TTFTB ligand coordinated to Zn^{2+} nodes (denoted as the 1-layer model; Fig. 1c), and the fully protonated H_4TTFTB ligand (Fig. 1d).

In the crystallized material, the TTFTB ligands overlap with a screw axis bisecting the ethylene bonds in TTFTB, giving a helical repeating pattern where the adjacent TTFTB ligands are rotated 60° with respect to one another.[42] A previous study suggested that ground state conductivity in the MOF was provided by S–S overlap between the ligands – a through-space

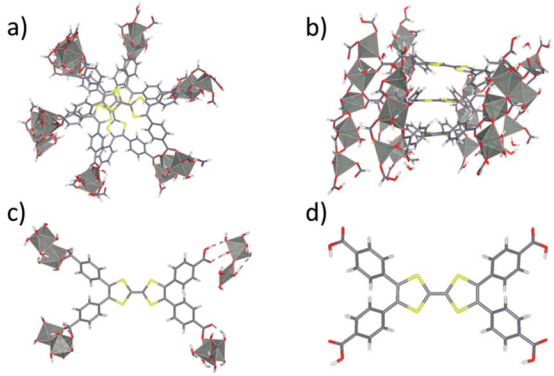

Fig. 1 Depiction showing a top (a) and side (b) view of the 3-layer model of Zn_2TTFTB conductive MOF in this study. The 3-layer cutout shown is half an optimized unit cell where each layer rotates 60° about the center. The 1 layer cut from an optimized unit cell (c) and the protonated ligand H_4TTFTB (d) are shown.

charge transport mechanism that does not rely on covalent interactions.[42] We investigate the mechanisms of excited state inter-layer and interfacial charge transport for the MOF as described in the section: Charge transport in Zn_2TTFTB.

The Zn_2TTFTB MOF has been traditionally synthesized by dissolving the H_4TTFTB ligand and Zn^{2+} ions in a heated DMF/ETOH/H_2O solution.[42] Here, it has been interfaced with the metal oxide to facilitate interfacial electron transfer. Solvothermal conditions were identified in which Zn_2TTFTB could be grown directly on FTO (fluorine-doped tin oxide), TiO_2, and ZrO_2 by adjusting the DMF : EtOH (dimethylformamide : ethanol) ratio, the concentrations of H_4TTFTB and Zn^{2+}, and by excluding excess H_2O from the solvent. Further synthetic details are provided in the Experimental section of the ESI.† In these studies, FTO functions as a transparent conductive substrate and Zn_2TTFTB–FTO is used for electrochemical and photoelectrochemical investigations of the MOF layer. Zn_2TTFTB–TiO_2 has a mesoporous layer of TiO_2 on top of the conductive FTO substrate and acts as a photoanode. Zn_2TTFTB–ZrO_2 is prepared similarly to TiO_2 and acts as a control in photophysical studies, utilizing ZrO_2 as a non-injecting medium.

The formation of Zn_2TTFTB on the substrates was confirmed using both pXRD and EXAFS at the Zn K-edge, providing both bulk and local structure information. The pXRD results are shown in Fig. 2a. The calculated pXRD pattern is based on the reported single crystal structure.[42] On all three substrates, the main diffraction features of Zn_2TTFTB (peaks at 9.3° and 10.2° 2θ) are observed and are well-isolated from the substrate pXRD diffraction patterns (Fig. S1†), suggesting that pure phase Zn_2-TTFTB is formed. While synthesis conditions can be adjusted to yield thicker films that more strongly diffract, the roughly 20 μm films investigated herein (*vide infra*) only diffract weakly, necessitating a more thorough structure investigation to confirm that the various synthetic conditions employed do not alter the structure.

X-ray absorption at the Zn K-edge was used to investigate the local structure of Zn^{2+} ions in four samples. The "Powder" sample is the sample prepared under the previously reported

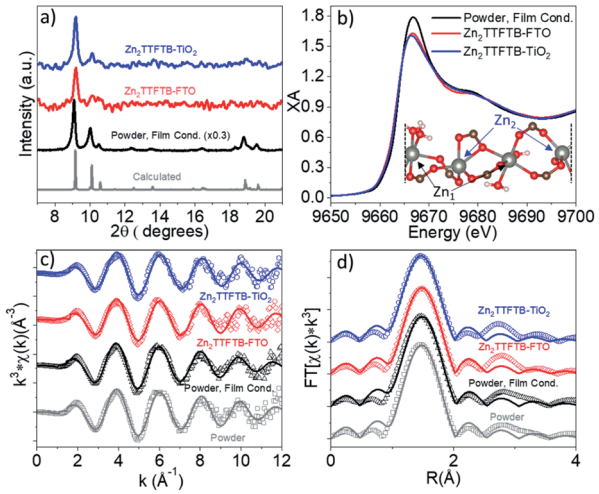

Fig. 2 Low 2θ region of the pXRD pattern containing Zn_2TTFTB diffractions (a) and Zn K-edge XANES spectra (b). EXAFS spectra in *k*-space (c) and *R*-space (d) with data shown as open points and solid best fit lines. Inset of (b) shows a segment of the MOF structure depicting the two unique Zn centers repeating in a chain.

synthetic procedure without modification[42] whereas "Powder, Film Cond." is prepared under the conditions used when growing the MOFs on the films (without the addition of excess H_2O to the reaction mixture and with a larger Zn : TTFTB ratio).

These two preparations give identical bulk structure *via* pXRD (Fig. S2a†). The Zn K-edge XANES and EXAFS spectra of these samples are compared in Fig. S2b–d† and are nearly identical implying similar local structure about Zn^{2+}. The powder spectra are compared to $ZnNO_3 \cdot 6H_2O$ reference data in Fig. S3.† The powder XANES spectrum is compared to the spectra of Zn_2-TTFTB–FTO and Zn_2TTFTB–TiO_2 in Fig. 2b wherein similar edge position is observed along with similar oscillation features above the 1s-4p transition edge. The white line of the edge transition at 9.667 keV shows attenuation in the Zn_2TTFTB–FTO and Zn_2-TTFTB–TiO_2 likely due to self-absorption, as fluorescence detection was required for the film samples whereas transmission mode was used for powder samples.

The EXAFS data were quantitatively analyzed with FEFF fitting using the Demeter package to compare the first shell local structure of the samples.[62] The *k*-space results and *R*-space results for each sample are compared in Fig. 2c and d, respectively. The input model for the FEFF calculation was prepared from the reported crystal structure coordinates.[42] In the crystal structure, there are two nonequivalent Zn atoms. One of these Zn atoms, Zn_1, has pseudo-octahedral coordination to six oxygen atoms, four of which are from carboxylate-bearing TTFTB ligands and two are water molecules. Zn_2 has five oxygen neighbors in its distorted octahedral first shell (including all atoms with a Zn–O distance of less than roughly 2.3 Å). Zn_2 has another O neighbor at about 2.7 Å that was considered to be in the second shell and therefore was not included in the fit model. A depiction of the Zn centers in a segment of the crystal structure is shown in the inset of Fig. 2b. Two separate FEFF calculations were performed and weighted at 50% in the analysis to incorporate the contributions of Zn_1 and Zn_2 to the data, which are each present at 50% in the crystal structure. It is worth noting that the self-absorption phenomenon observed in film samples attenuates the oscillations throughout the EXAFS spectrum and results in reduction in amplitude of the Fourier-transformed *R*-space spectra, typically contributing to the Debye–Waller parameter (σ^2) that accounts for static and dynamic disorder, but does not affect the distances obtained from quantitative EXAFS analysis.

Results of EXAFS fitting are shown in Table 1. As noted, σ^2 is in general larger for the film samples compared to the powder samples most likely due to self-absorption attenuation and not due to a physically relevant reason. The observed Zn–O distances are within uncertainty (±0.02 Å) between samples implying that the films have the same local structure as the powder samples. Interestingly, the distances observed from EXAFS analysis are shorter than those from the reported crystal structure. This is potentially because the reported bulk synthesis method (which produces particles on the order of 10 μm × 3 μm)[54] differs from the reported synthesis to grow larger X-ray crystallography quality crystals.[42]

With confirmation that the Zn^{2+} ions measured on films have local structure consistent with Zn_2TTFTB formation, SEM was used to investigate the morphology of the samples. Synthesis of powder samples under the film-growth conditions produces a particle morphology that differs significantly from that when using the reported synthesis method (Fig. S4†), and the morphology of the MOF on films differs from either of the powder morphologies. Fig. 3 shows the SEM images for Zn_2-TTFTB–TiO_2. The top-view images (Fig. 3a and b) show that

Table 1 Zn K Edge EXAFS fit results. ΔE_0 is the energy shift, σ^2 is the Debye–Waller parameter, *R* is the ZnO distance, S_0^2 is the amplitude factor and *N* is the coordination number. Uncertainty in *R* is ±0.02 Å; uncertainty in σ^2 is ±0.001 Å^2. Crystal ref. distances from Narayan T. C. *et al.*[42]

Description/shared				Powder			Powder, film cond.			Zn_2TTFTB–FTO			Zn_2TTFTB–TiO_2		
Vector	Ref. (Å)	*N*	S_0^2	ΔE_0 (eV)	σ^2 (Å^2)	*R* (Å)	ΔE_0 (eV)	σ^2 (Å^2)	*R* (Å)	ΔE_0 (eV)	σ^2 (Å^2)	*R* (Å)	ΔE_0 (eV)	σ^2 (Å^2)	*R* (Å)
Zn_1–O	2.06	3	0.5	4.36	0.002	2.03	4.04	0.001	2.04	3.42	0.004	2.03	3.38	0.002	2.03
	2.12	2				2.09			2.10			2.09			2.09
	2.17	1				2.14			2.14			2.13			2.13
Zn_2–O	1.95	1	0.5	8.52	0.001	1.91	7.64	0.001	1.91	10.00	0.002	1.93	9.35	0.001	1.91
	1.98	2				1.94			1.94			1.96			1.94
	2.04	1				2.00			1.99			2.02			2.00
	2.33	1				2.29			2.29			2.31			2.29

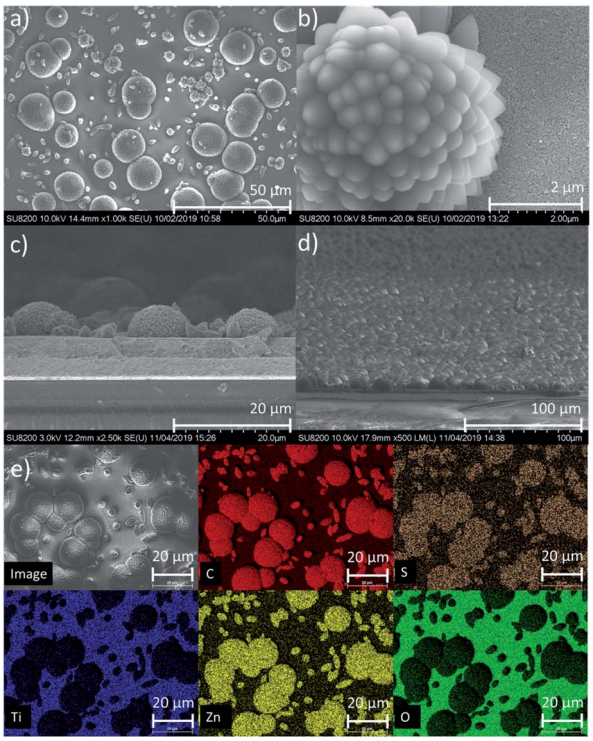

Fig. 3 SEM results for Zn_2TTFTB–TiO_2. Top-view images (a and b) and cross-section images (c and d) show the formation of a discontinuous monolayer of hemispherical flower-like MOF structures. EDS mapping (e), demonstrating localization of C, S, and Zn within the MOF structures. Scales: (a) 50 μm; (b) 2 μm; (c) 20 μm; (d) 100 μm; (e) 20 μm.

there are MOF structures of larger (roughly 20 μm) and smaller sizes decorating the surface of the mesoporous TiO_2 film. The larger particles form microflowers that are shown to be hemispherical from the side-view cross-section image (Fig. 3c) and evenly cover the surface of TiO_2 from a tilted perspective (Fig. 3d). Zn_2TTFTB–FTO was found to have the same morphology (Fig. S5†). EDS results show the expected localization of Zn, S, and C within the MOF structures (Fig. 3e). The morphology of Zn_2TTFTB on films is therefore best described as a discontinuous monolayer of hemispherical microflower structures.

UV-visible Electronic Characterization

Tetrathiafulvalene is well known to display redox-state dependent UV-visible absorption features.[63–65] Therefore, we compare the spectroelectrochemical properties of the H_4TTFTB ligand and Zn_2TTFTB MOF (*i.e.* Zn_2TTFTB–FTO). The H_4TTFTB sample was dissolved in 0.1 M $TBAPF_6$ DMF electrolyte ($TBAPF_6$ is tetrabutylammonium hexafluorophosphate, the supporting electrolyte) for cyclic voltammetry experiments. Two reversible oxidation features are observed (Fig. 4a, inset) for H_4TTFTB, and no reversible features are observed on the reduction side (Fig. S6†). Therefore, spectroelectrochemistry was performed to target the reversible features for oxidation, and reduction was performed in steps between 0 V and −1.5 V. Fig. 4a shows the spectroelectrochemical oxidation of H_4TTFTB. Upon the first

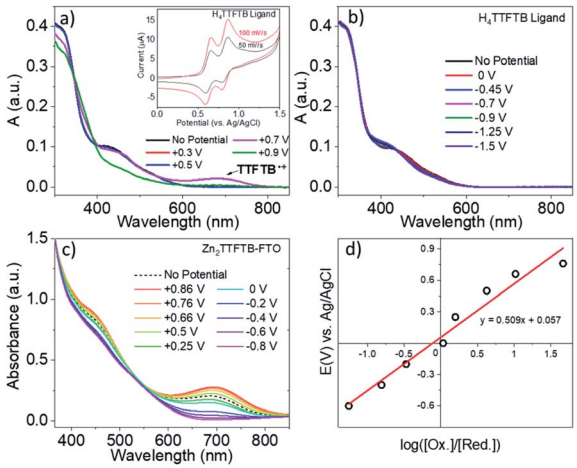

Fig. 4 (a) Spectroelectrochemistry of H_4TTFTB under oxidation and (b) reduction. (c) Spectroelectrochemistry of Zn_2TTFTB–FTO. (d) Nernst plot of Zn_2TTFTB–FTO spectroelectrochemistry data at 700 nm. Inset of (a) is the cyclic voltammetry of H_4TTFTB in 0.1 M $TBAPF_6$-DMF.

oxidation at +0.7 V *vs.* Ag/AgCl, a broad absorption feature is observed in the region between 600–800 nm. This feature is in excellent agreement with the cation radical spectrum of closest reported structure, the ethyl ester derivative.[66] The second oxidation at +0.9 V depletes this feature and causes further spectral changes. Reduction (Fig. 4b) results in more subtle changes in the <600 nm region of the spectrum but has no clear changes beyond 600 nm where oxidation displays a clear feature.

Unlike H_4TTFTB, Zn_2TTFTB–FTO does not show clear signatures under cyclic voltammetry conditions; however, the high optical quality of the films allowed transmission mode spectroelectrochemical measurements to be made. The spectroelectrochemical results in 0.1 M $TBAPF_6$ DMF show that prior to applying a bias, an absorption feature is present in the 600–800 nm region (Fig. 4c, "No Potential"). Upon the application of oxidizing potentials, growth of the feature is observed along with changes in the 400–500 nm region. When reducing potentials are applied, both of these features are depleted and the feature between 600–800 nm disappears completely. The ΔA spectra shown in Fig. S7† demonstrate that similar absorption changes are observed in H_4TTFTB compared to Zn_2TTFTB in the region above 500 nm. These results indicate that a well-resolved spectral signature of the MOF cation exists in the 600–800 nm region of the spectrum that is absent in both the neutral and reduced species.

A Nernst plot was generated utilizing this feature at 700 nm in the spectroelectrochemistry data (Fig. 4d) yielding an E_0 value of 57 mV and an *n*-value of 0.15 from the slope corresponding to the number of electrons transferred. TTF polymer films have been previously studied *via* Nernst analysis where similar results were obtained, *i.e.* a redox potential for the first oxidation lower than that of the monomer and an *n*-value less than one.[65,67] In other conductive polymer systems, an *n*-value lower than unity has also been observed and attributed to its being

a per-monomer measure of the redox process.[68,69] In such systems, there exists the possibility for oxidation events that are delocalized or, in the case of TTF, cation dimers have been observed implying that the cation may be localized on adjacent TTF units.[65,67] These points are further investigated in the section: Charge transport in Zn_2TTFTB.

As noted above, Zn_2TTFTB–FTO has a clear absorption feature in the region of the cation absorption prior to applying a potential. As-synthesized, Zn_2TTFTB has a brown-red color that has been previously reported as early as 1970 in solid tetrathiafulvalene powders exposed to oxygen.[63] It has also been demonstrated experimentally *via* EPR that Zn_2TTFTB contains radicals.[42] In agreement with the Zn_2TTFTB–FTO spectrum, the diffuse reflectance UV-visible spectrum of Zn_2TTFTB powder also shows the cation feature between 600–800 nm (Fig. 5a). The solid H_4TTFTB powder also has this feature (Fig. S8†). However, when H_4TTFTB is dissolved in DMF, the solution becomes a deep orange color and no longer shows the absorption feature between 600–800 nm (Fig. 5a). It appears that both the Zn_2-TTFTB MOF and H_4TTFTB powders are oxidized in air to become partially cation doped. This is likely, in part, due to the formation of a stabilized radical dimer[65] or other stabilized cation species.

To further investigate this hypothesis and to gain insight into the nature of the observed UV-visible features, we performed time-dependent density functional theory (TDDFT) calculations (Fig. 5) to examine the dependence of the absorption spectrum on the redox state of H_4TTFTB. The neutral, cationic, anionic, and dicationic states of H_4TTFTB were considered in a DMF environment using the polarizable continuum model (PCM).[70] The experimental data from spectroelectrochemistry experiments is used for comparison to the computational results. The calculated UV-visible absorbance of the neutral H_4TTFTB ligand is in reasonable agreement with the experimental spectra with each containing a prominent band and a shoulder that extends into the visible region of the spectrum. While the shape of the features in the experimental spectrum is reproduced, the entire spectrum appears to be blue-shifted with respect to the experimental spectrum. The Natural Transition Orbitals (NTO's) of the 426 nm peak (Fig. 5a) show a delocalization from the TTF core to the peripheral phenyl groups upon excitation.

Difference spectra between the cation and neutral species, and anion and neutral species are shown in Fig. 5b and c, respectively, for both the calculated and experimental spectra. The calculated cation difference spectrum shows good agreement with the experimental spectrum. Peak 2 in the calculated spectrum is found at 433 nm and underlies the broad band at 370 nm compared to the experimental location of 475 nm. Peaks 2 and 3 in the cationic difference spectra are attributed to delocalization transitions across the molecule while peak 1 remains localized. The broad peak 3 from approximately 500 nm to beyond 1000 nm is also consistent with the absorption feature in this region observed experimentally (Fig. 5b). The calculated anionic difference spectrum (Fig. 5c) also showed good agreement with the experimental spectrum. Peak 1 for this difference is attributed to movement of density away from the TTF core, while peak 2 shows greater localization onto the core. However, the experimental observation of only a slight increase in the anionic spectrum as compared to the neutral spectrum in

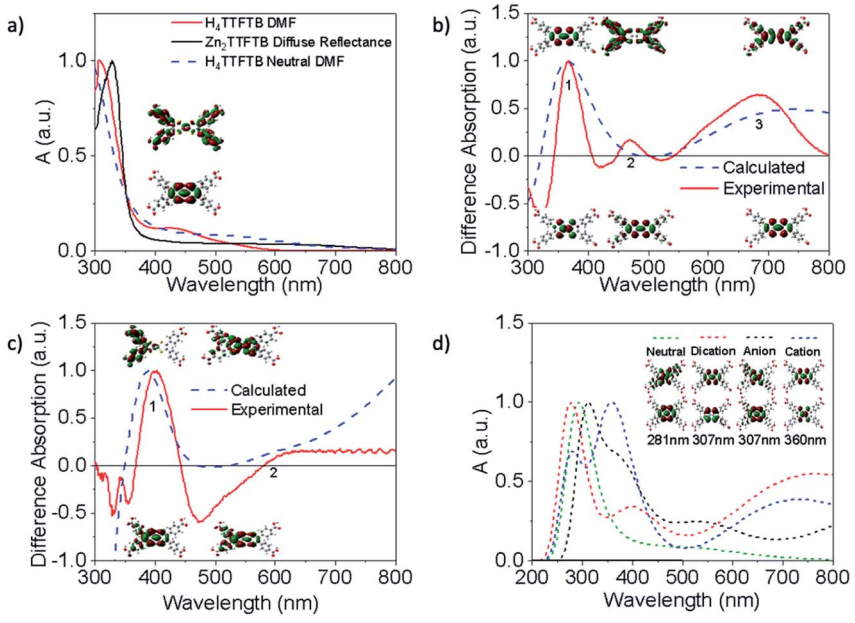

Fig. 5 Experimental (solid) and calculated (dashed) normalized UV-visible spectra. Stacked Natural Transition Orbitals (NTOs) show the initial (bottom) and final (top) orbitals for each transition. (a) UV-visible spectrum of H_4TTFTB in DMF compared to the diffuse reflectance spectrum of Zn_2TTFTB and the calculated neutral ligand in DMF with NTO's for the transition of interest. (b and c) Difference spectra comparison of the experimental and TDDFT calculated H_4TTFTB cationic-neutral/anion-neutral species spectra and the NTO's of important features. (d) Comparison of TDDFT calculated spectra for charge varied species and NTO's for the same transition in each species.

the 600–800 nm region suggests the anion is not responsible for extended shoulder seen in the MOF diffuse reflectance spectrum (Fig. 5a)

Calculated spectra for the neutral, anion, cation, and dication species are overlaid in Fig. 5d and are seen to have a visible shift in dominant peaks, and the appearance of multiple peaks in the charged spectra. To ensure the same feature was being analyzed between each spectrum, the NTO's for vibrations found in the region of the dominant peak were analyzed. The NTO's with the greatest similarity to the neutral 281 nm transition, which was found to be isolated from other peaks in the spectrum and therefore clearly the sole originator of the intensity, were selected and are shown in Fig. 5d. These features all largely remain localized on the TTF core and do not contribute to the delocalized shoulder feature. Additional discussion about the ordering of the peaks can be found in the ESI.† Additional NTO's for each of the charged and neutral species are shown in Fig. S9 and S10.† To investigate whether ligand stacking produces a feature in the 600–800 nm region, a 2-layer model was utilized (Fig. S11†) rather than the half-unit cell 3-layer model due to computational constraints. Absorption spectra in Fig. S12† demonstrate that while simple stacking of the layers does show a broadening of the 300 nm peak, simple stacking does not lead to a new absorption band between 600–800 nm as is seen experimentally in the full MOF or the cationic systems. Therefore, it becomes clear that the 600–800 nm band is entirely a product of cation doping.

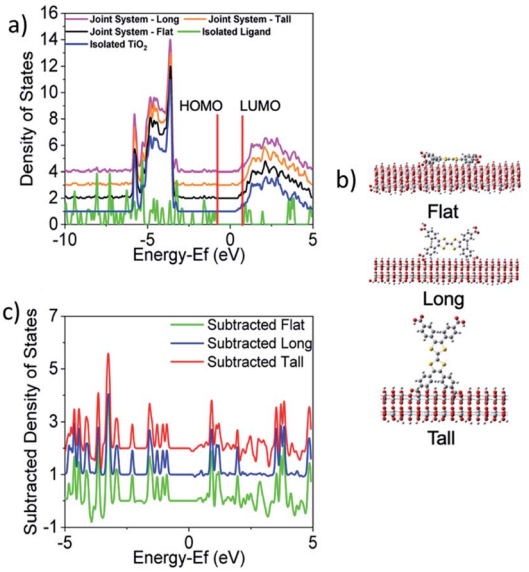

Fig. 6 The (a) calculated density of states (DOS) are shown for TTFTB lying (b) flat, long, or tall on the surface, each with 2 attachment points. The HOMO and LUMO positions of the isolated ligand are denoted in red. Full DOS for each joint system orientation are overlaid with the isolated ligand and isolated TiO_2 DOS. All DOS containing TiO_2 which have been vertically scaled to a maximum peak height of 10. (c) Subtraction of the joint systems from the summation of isolated systems shows the changes in the DOS when the ligand is bound to TiO_2. (a) and (c) are both centered on the Fermi level of the joint flat system.

Zn_2TTFTB as a photosensitizing array

Given an understanding of both the optical properties and energetics of Zn_2TTFTB, we investigated the conductive MOF film as a photosensitizer. In this scenario, visible light is absorbed by the photosensitizer followed by injection of an electron into the conduction band of TiO_2. The UV-vis results demonstrated that the excitations are mainly ligand-centered, and this finding is unsurprising given that the metal oxide nodes of the MOF are composed of d10 Zn^{2+} ions. Therefore, the energetics of electron injection from Zn_2TTFTB to TiO_2 was modeled based on the TTFTB ligand as a computationally-feasible model system. TTFTB has four carboxylate groups, leading to various possibilities for attachment to the metal oxide surface. It is noted that one or more of these binding geometries could contribute to the model system and also to the Zn_2TTFTB–TiO_2 system, as the exact binding mode between Zn_2TTFTB and TiO_2 is uncertain.

Taking these potential binding geometries into account, three models were created on a periodic TiO_2 slab to investigate the density of states (DOS) with details on model formation and calculation in the ESI.† Their binding geometries are denoted flat, long, or tall (Fig. 6). The calculated DOS are presented in Fig. 6 showing the joint system DOS with the ligand in the three binding geometries as well as the isolated ligand and isolated TiO_2 DOS. All density of states are shifted by the Fermi level of the joint flat system and were aligned to experimental values following the procedure outlined in the ESI.† The HOMO of the ligand is found to be within the bandgap of TiO_2 whereas the LUMO is found to be slightly above the conduction band edge of isolated TiO_2 (located at 0.21 eV), implying energetic favorability for electron injection. The strong interaction between the ligand and TiO_2 can additionally be seen in the subtracted density of states shown in Fig. 6c where the DOS of the joint systems have each been subtracted from the summed DOS of the isolated ligand and surface. This figure shows that upon binding, the ligand and TiO_2 interact to cause changes in the DOS up to as large as a third of the height of the maximum peak.

To investigate the electron injection process computationally, interfacial electron transfer (IET) calculations were performed for the tall, long, and flat orientations of the ligand on TiO_2. Survival probabilities of an electron in the ligand, shown in Fig. S13,† support the experimental result to follow suggesting electron injection occurs in less than the instrument response function of 0.6 ps. Snapshots of the injection from each orientation are shown in Fig. 7 and movies can be viewed in the ESI.† At 0 fs, the LUMO density lies fully on the ligand. At later times, such as 27 fs, some density has moved from the ligand to the TiO_2 slab for all orientations. The density spreads out horizontally into the periodic slab or is absorbed by an absorbing boundary condition at the bottom of the slab.

A well-established technique for experimentally investigating carrier injection and subsequent trapping/recombination dynamics in sensitized metal oxides is optical-pump THz-probe spectroscopy (OPTP). It has subpicosecond time resolution and is sensitive to mobile carriers, such as

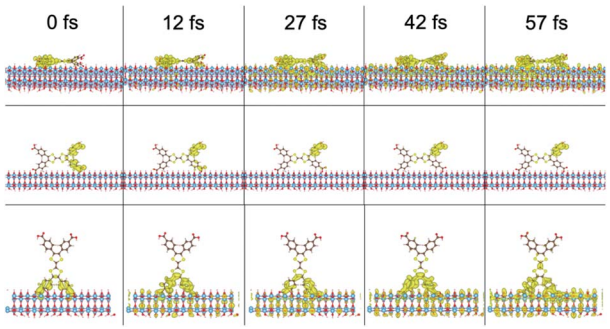

Fig. 7 Interfacial electron transfer from H_4TTFTB on TiO_2 in a flat (top), long (middle), and tall (bottom) orientation.

conduction band electrons, making it a non-contact probe for studying transient photoconductivity.[71] As a result, OPTP has been widely applied to study dye-sensitized metal oxide systems.[15,32,72–75] As indicated by our theoretical investigations, the carboxylate-bearing TTFTB ligand is energetically poised to photoinject electrons into TiO_2. Therefore, TTFTB-sensitized samples were studied alongside Zn_2TTFTB–TiO_2 samples to compare how injection and/or recombination dynamics differ in the presence of an extended structure of overlapped chromophores, such as in Zn_2TTFTB. The UV-visible spectra of these samples are shown in Fig. S14.†

OPTP was performed on Zn_2TTFTB–TiO_2, TTFTB-sensitized TiO_2, and, as a control to probe the intrinsic MOF photoconductivity on a non-injecting metal oxide, Zn_2TTFTB–ZrO_2. The samples were prepared on quartz substrates and photoexcited at 400 nm using various pump fluences as shown in Fig. 8. In our previous work, the optical penetration depth for Zn_2TTFTB at 400 nm was determined to be about 7 μm, which is on the order of the largest radius of hemispherical MOF features observed (Fig. 3c).[54] As the optical penetration depth is defined as the distance at which incident radiation intensity decays to 1/*e* (about 37%), the MOF features can be excited throughout their structure, even at their largest radii. TTFTB-sensitized TiO_2 (Fig. 8a) shows an onset of THz attenuation that is limited by the instrument response function (IRF) of 600 fs due to electron injection into mobile conduction band states of TiO_2. It is followed by a decay that is the result of trapping and recombination processes that depopulate the conductive states. The IRF-limited injection is supported by the computational IET results that show injection on a <100 fs timescale. Transients of a similar profile and degree of THz attenuation are seen with Zn_2TTFTB–TiO_2 (Fig. 8b), implying that Zn_2TTFTB is also a suitable photosensitizer. A plot of the peak THz attenuation as a function of pump fluence shows that the THz attenuation scales linearly with pump fluence (Fig. S15†). When the control Zn_2TTFTB–ZrO_2 is measured under the highest fluence (1.27 mJ cm^{-2}), a very small signal is observed that is over an order of magnitude weaker than that for Zn_2TTFTB–TiO_2. The signal from the Zn_2TTFTB–ZrO_2 film (Fig. S16†) is due to the intrinsic photoconductivity of Zn_2TTFTB as we reported previously,[54] and its negligible contribution to the injection signal is not considered in modeling.

The trapping and recombination processes observed in the timescale of OPTP experiments are inherently heterogeneous resulting in such processes occurring on a range of timescales. This has been previously accounted for with a stretched exponential model that results in modelling the exponential decay with a distribution of time constants described by the exponential term β.[72] The fit model for OPTP data is given by eqn (1):

$$-\Delta\mathrm{THz} = \left[A\mathrm{e}^{\left(-\frac{t_{\mathrm{pump}}}{\tau}\right)^{\beta}} + y_0\right] \otimes G_{\mathrm{R}}(\mathrm{fwhm}) \quad (1)$$

The amplitude of the stretched exponential is given by A. The post-decay offset, y_0, accounts for remaining signal at the end of the measurable time range. The stretching factor β is fixed at 0.3 to allow straightforward comparisons of the fitted stretched time constants (τ). The stretched exponential with offset is convoluted with a Gaussian IRF with a fixed value of 0.6 ps.

The fit results are shown in Table 2. The time constants increase as a function of pump fluence, which we ascribe to band filling and trap state filling with increased electron density. The electron densities are not large enough to result in

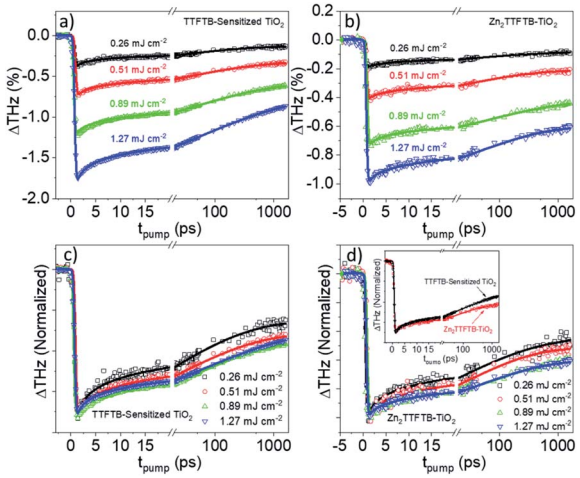

Fig. 8 OPTP traces for TTFTB-sensitized TiO_2 (a) and Zn_2TTFTB (b) and their respective normalized traces (c and d). Inset of (d) compares the normalized TTFTB-sensitized trace to the Zn_2TTFTB–TiO_2 trace at 1.27 mJ cm^{-2} excitation fluence.

Table 2 OPTP best fit results using eqn (1) for ligand-sensitized TTFTB–TiO_2 and MOF-sensitized Zn_2TTFTB–TiO_2

Sample	Fluence	IRF (ps)	τ (ps)	A	β	Y_0 decay offset
TTFTB–TiO_2	0.26	0.6	15.3 (0.4)	−0.34	0.3	−0.13
	0.51		21.3 (0.3)	−0.57		−0.32
	0.89		34.0 (0.3)	−0.85		−0.58
	1.27		35.0 (0.4)	−1.32		−0.82
Zn_2TTFTB–TiO_2	0.26	0.6	12.5 (0.3)	−0.17	0.3	−0.09
	0.51		18.2 (0.2)	−0.30		−0.21
	0.89		39.0 (0.3)	−0.42		−0.42
	1.27		37.2 (0.4)	−0.51		−0.57

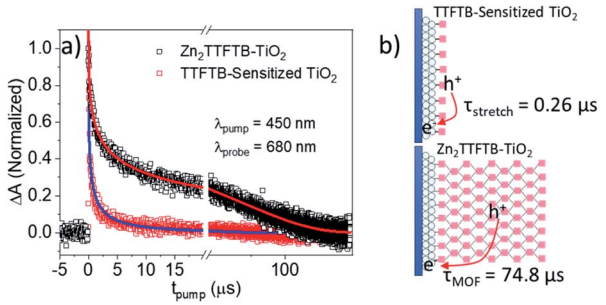

Fig. 9 (a) ns-TA results showing the recombination lifetime and (b) proposed scheme.

higher-order recombination processes, however, as these processes would result in a decrease in the observed time constants as a function of pump fluence and would also cause deviation from linearity in the THz attenuation as a function of pump fluence, which is not observed (Fig. S15†).

In comparing the normalized traces in the pump fluence regime where the dynamics were not fluence dependent for TTFTB-sensitized TiO_2 and Zn_2TTFTB–TiO_2 (Fig. 8d, inset), it is observed that, especially on longer timescales, Zn_2TTFTB–TiO_2 deviates from TTFTB-sensitized and has a slower decay, which is corroborated by the fitted time constants. Additional comparisons were made (Fig. S17†) between data sets with similar ΔTHz magnitudes in both the regimes of fluence-dependent dynamics and fluence-independent dynamics yielding the same trend that the Zn_2TTFTB signal is longer-lived. On longer timescales, it is expected that these dynamics are related to recombination of the electron in the TiO_2 conduction band with the hole on the photosensitizer.

In order to compare the recombination dynamics between MOF-sensitized Zn_2TTFTB–TiO_2 and TTFTB-sensitized TiO_2 on a longer timescale, we took advantage of the well-resolved TTFTB cation feature between 600–800 nm using nanosecond transient absorption (ns-TA) experiments. Upon electron injection into TiO_2 using 450 nm excitation, a transient cation is formed on TTFTB or Zn_2TTFTB which was probed at 680 nm. From the normalized TA data in Fig. 9a, it is clearly observed that Zn_2TTFTB–TiO_2 has a longer lifetime for the transient cation feature indicating delayed recombination with respect to TTFTB-sensitized TiO_2 (Table 3).

The TTFTB-sensitized TiO_2 transient was modeled with a stretched exponential (eqn (2)) to account for heterogeneity in the recombination process. The fit shown in Fig. 9a adequately describes the decay dynamics and a time constant of 0.26 μs is obtained. If the same model is used for the Zn_2TTFTB-sensitized sample, then adequate agreement cannot be obtained (Fig. S18†). Therefore, a longer-lived single exponential contribution was added (eqn (3)) and used to fit the Zn_2TTFTB–TiO_2 data. Very good agreement is obtained, and the time constant for the long-lived component is 74.8 μs. The stretched time constant ($\tau_{stretch}$) was also found to be larger for Zn_2TTFTB–TiO_2.

Table 3 ns-TA fit results using eqn (2) and (3)

Sample	$A_{stretch}$	$\tau_{stretch}$ (μs)	β	A_{MOF}	τ_{MOF} (μs)
TTFTB–TiO_2	1.09	0.26	0.35	—	—
Zn_2TTFTB–TiO_2	0.94	1.43	0.35	0.22	74.8

$$\Delta A = A_{stretch} e^{\left(\frac{-t_{pump}}{\tau_{stretch}}\right)^{\beta}} \quad (2)$$

$$\Delta A = A_{stretch} e^{\left(\frac{-t_{pump}}{\tau_{stretch}}\right)^{\beta}} + A_{MOF} e^{\left(\frac{-t_{pump}}{\tau_{MOF}}\right)} \quad (3)$$

These ns-TA results are in agreement with OPTP results and show that recombination of the interfacially-separated electron–hole pair is significantly slower in the MOF-sensitized Zn_2TTFTB–TiO_2 system compared to the TTFTB-sensitized TiO_2 system. Given the extended conductive MOF structure in Zn_2TTFTB, a scheme is proposed in Fig. 9b to explain this result. In TTFTB-sensitized TiO_2, the TTFTB-localized hole is constrained to the surface of TiO_2 where it can recombine with the electron in TiO_2. In the MOF system, however, this is not the case. Due to the MOF's conductivity, the hole is mobile and not restricted to the surface. In addition, the instrument-response limited electron injection observed may involve injection from more distant TTFTB chromophores of the MOF that are not directly linked to the surface. It takes much longer for the hole to diffuse to the interface and recombine with the electron compared to TTFTB-sensitized samples where it is constrained to be at the interface. Thus, the Zn_2TTFTB MOF photosensitizer acts as a photosensitizing array that can separate the electron–hole pair to inhibit recombination.

Charge transport in Zn_2TTFTB

Computational and experimental results in the UV-visible electronic properties section implied that the UV-visible absorption of both the cation and the neutral oxidation states are ligand-centered in Zn_2TTFTB. This point was further investigated by calculating the spin density of the radical cationic forms of H_4TTFTB and the 1 layer model (Fig. 10). From the figure, it is clear that the hole is localized on the central S-containing rings of the TTFTB ligand. The molecular orbitals for the HOMO, LUMO, and LUMO+1 for both the 1 layer and 3 layer models were calculated and are shown in Fig. S19.† The HOMO appears to localize on the central S-rich region of TTFTB while the near-degenerate LUMO and LUMO+1 localize on the phenyls of the system. These results imply that upon photoexcitation, the photogenerated hole will localize on the S-rich central region of TTFTB while the electron will localize to the peripheral phenyl rings, thereby giving the hole and electron separate transport pathways within the MOF structure. The localization of the electron on the periphery is further supported by the calculated NTOs of H_4TTFTB (Fig. S9†).

To further explore the proposed charge transport mechanism, time-evolution of the inter-layer electron and hole dynamics upon photoexcitation were simulated at the extended Hückel level of

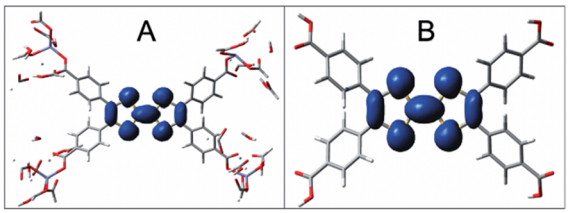

Fig. 10 Spin densities of the cationic H_4TTFTB and 1 layer models. Spin density is represented in blue and is seen on the tetrathiafulvaline core only for an isovalue of 0.0008 for 1 layer Zn_2TTFTB (A) and H_4TTFTB (B).

theory (Fig. S20 and S21†). Wavepackets for the electron and hole were initialized in the LUMO and HOMO, respectively for each layer of a model composed of six TTFTB ligands oriented as in the crystallographic unit cell of the MOF. The wavepackets were propagated along the configurations sampled by four independent molecular dynamics trajectories at a DFT tight binding level of theory. The simulations revealed that the hole propagates through the tetrathiafulvalene cores at the center of the columnar stack with rates comparable to or greater than the photo-excited electron, which travels through the spiraling staircase of phenyl substituents on the periphery of the structure (Fig. 11). The photo-generated hole generally becomes more delocalized between ligand layers than the electron. These calculations are in agreement with the spectroelectrochemistry results in the "UV-visible electronic characterization" section and support a delocalized hole species as opposed to a strictly dimeric species.

The wavepacket dynamics results (Fig. S20–S22†) suggest a difference in the inter-layer electronic coupling for the frontier orbitals. In fact, the HOMO–HOMO coupling for hole transport was computed to be 2.7–4.5 times larger on average than the LUMO–LUMO coupling for electron transport (Fig. S22†), a result that is consistent with the different extents of spatial overlap for these orbitals. Taken together, the wavepacket dynamics and electronic coupling calculations indicate that photo-generated electrons and holes are transported through spatially distinct pathways that afford holes much greater inter-layer mobility.

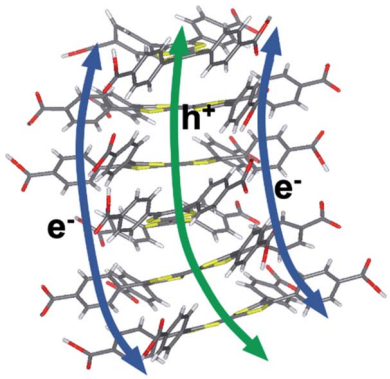

Fig. 11 Proposed electron and hole transfer pathways. Calculations in this work suggest that electrons travel between phenyl stacks and holes through the S-rich TTF core.

For both electrons and holes, the inter-layer transfer is predicted to take place within 200 fs upon photoexcitation, consistent with the instrument-response limited timescale measured experimentally for injection into TiO_2. The intrinsic photoconductivity of the MOF suggests that the injected charge may originate from layers proximal or distal to the interface. In either case, the accelerated mobility of holes over electrons along the constrained channels in the MOF provides a mechanistic interpretation of the slower charge recombination observed experimentally for the MOF, as opposed to single ligand sensitized TiO_2 surfaces. The results suggest a model wherein the ultrafast injection of the photo-generated electron is complemented by the rapid migration of the hole through the ligand rungs of the columnar stack away from the interfacial region. The ability to affect charge separation due to the different pathways for electron and hole conductance in the MOF (Fig. 11) can be exploited for artificial photosynthesis and photooxidation catalysis due to extended hole lifetime and the opportunity to rationally interface catalytic moieties directly within the hole transport pathway to strongly couple the catalyst to the photogenerated hole in the MOF photosensitizing array.

Conclusions

We have introduced a conductive MOF-sensitized TiO_2 photoanode with photoconductivity properties particularly suitable for photocatalytic applications. We find that photoexcitation of Zn_2-TTFTB–TiO_2 leads to efficient electron–hole pair separation, with holes migrating through the S-rich TTFTB cores while the electrons transfer through the peripheral phenyl groups. Time-resolved THz OPTP experiments indicate ultrafast electron injection into TiO_2, leaving holes on the conductive Zn_2TTFTB MOF photosensitizing array. The HOMOs of the TTFTB ligands are highly coupled, resulting in efficient transport of the photogenerated holes through the S-rich cores of the MOF. The ligand LUMOs are weakly coupled, and localized on the phenyl substituents. Nevertheless, both types of carriers (*i.e.*, electrons and holes) are mobile and contribute to the efficient charge separation. In fact, our nanosecond transient absorption experiments have shown that the photogenerated hole feature has a much longer lifetime (at least two orders of magnitude longer) than in the ligand-sensitized TiO_2 that lacks the extended MOF structure. Given these results, there is great promise in developing conductive MOF photoanode architectures for performing slow and thereby difficult oxidation reactions.

Conflicts of interest

There are no conflicts to declare.

Acknowledgements

This work was supported by the U.S. Department of Energy, Office of Science, Office of Basic Energy Sciences, under award DE-FG02-07ER15909, as well as from a generous donation from the TomKat Foundation. R. O. acknowledges funding from the Nakatani Foundation for performing research at Yale University

in the Schmuttenmaer group. V. S. B. acknowledges high-performance computing time from NERSC.

References

1 A. J. Bard and M. A. Fox, *Acc. Chem. Res.*, 1995, **28**, 141.
2 T. J. Meyer, *Acc. Chem. Res.*, 1989, **22**, 163.
3 A. J. Esswein and D. G. Nocera, *Chem. Rev.*, 2007, **107**, 4022.
4 X. Chen, S. Shen, L. Guo and S. S. Mao, *Chem. Rev.*, 2010, **110**, 6503.
5 Y. Tachibana, L. Vayssieres and J. R. Durrant, *Nat. Photonics*, 2012, **6**, 511.
6 I. McConnell, G. Li and G. W. Brudvig, *Chem. Biol.*, 2010, **17**, 434.
7 M. R. Wasielewski, *Chem. Rev.*, 1992, **92**, 435.
8 D. Gust, T. A. Moore and A. L. Moore, *Acc. Chem. Res.*, 1993, **26**, 198.
9 D. F. Watson and G. J. Meyer, *Annu. Rev. Phys. Chem.*, 2005, **56**, 119.
10 I. Robel, M. Kuno and P. V. Kamat, *J. Am. Chem. Soc.*, 2007, **129**, 4136.
11 M. Borgström, E. Blart, G. Boschloo, E. Mukhtar, A. Hagfeldt, L. Hammarström and F. Odobel, *J. Phys. Chem. B*, 2005, **109**, 22928.
12 J. Huang, O. Buyukcakir, M. W. Mara, A. Coskun, N. M. Dimitrijevic, G. Barin, O. Kokhan, A. B. Stickrath, R. Ruppert, D. M. Tiede, J. F. Stoddart, J.-P. Sauvage and L. X. Chen, *Angew. Chem., Int. Ed.*, 2012, **51**, 12711.
13 J. Kallioinen, G. Benkö, V. Sundström, J. E. I. Korppi-Tommola and A. P. Yartsev, *J. Phys. Chem. B*, 2002, **106**, 4396.
14 S. K. Cushing, J. Li, J. Bright, B. T. Yost, P. Zheng, A. D. Bristow and N. Wu, *J. Phys. Chem. C*, 2015, **119**, 16239.
15 G. M. Turner, M. C. Beard and C. A. Schmuttenmaer, *J. Phys. Chem. B*, 2002, **106**, 11716.
16 S. G. Abuabara, C. W. Cady, J. B. Baxter, C. A. Schmuttenmaer, R. H. Crabtree, G. W. Brudvig and V. S. Batista, *J. Phys. Chem. C*, 2007, **111**, 11982.
17 J. R. Swierk and T. E. Mallouk, *Chem. Soc. Rev.*, 2013, **42**, 2357.
18 P. Xu, T. Huang, J. Huang, Y. Yan and T. E. Mallouk, *Proc. Natl. Acad. Sci. U. S. A.*, 2018, **115**, 6946.
19 Y. Zhao, J. R. Swierk, J. D. Megiatto, B. Sherman, W. J. Youngblood, D. Qin, D. M. Lentz, A. L. Moore, T. A. Moore, D. Gust and T. E. Mallouk, *Proc. Natl. Acad. Sci. U. S. A.*, 2012, **109**, 15612.
20 G. F. Moore, J. D. Blakemore, R. L. Milot, J. F. Hull, H.-e. Song, L. Cai, C. A. Schmuttenmaer, R. H. Crabtree and G. W. Brudvig, *Energy Environ. Sci.*, 2011, **4**, 2389.
21 A. Fujishima and K. Honda, *Nature*, 1972, **238**, 37.
22 R. J. Kamire, K. L. Materna, W. L. Hoffeditz, B. T. Phelan, J. M. Thomsen, O. K. Farha, J. T. Hupp, G. W. Brudvig and M. R. Wasielewski, *J. Phys. Chem. C*, 2017, **121**, 3752.
23 W. J. Youngblood, S.-H. A. Lee, Y. Kobayashi, E. A. Hernandez-Pagan, P. G. Hoertz, T. A. Moore, A. L. Moore, D. Gust and T. E. Mallouk, *J. Am. Chem. Soc.*, 2009, **131**, 926.
24 Y. Gao, L. Zhang, X. Ding and L. Sun, *Phys. Chem. Chem. Phys.*, 2014, **16**, 12008.
25 L. Zhang, Y. Gao, X. Ding, Z. Yu and L. Sun, *ChemSusChem*, 2014, **7**, 2801.
26 A. K. Chandiran, M. K. Nazeeruddin and M. Grätzel, *Adv. Funct. Mater.*, 2014, **24**, 1615.
27 J. Nissfolk, K. Fredin, A. Hagfeldt and G. Boschloo, *J. Phys. Chem. B*, 2006, **110**, 17715.
28 N. Yao, J. Huang, K. Fu, X. Deng, M. Ding, S. Zhang, X. Xu and L. Li, *Sci. Rep.*, 2016, **6**, 31123.
29 L. Li, C. Xu, Y. Zhao, S. Chen and K. J. Ziegler, *ACS Appl. Mater. Interfaces*, 2015, **7**, 12824.
30 E. Palomares, J. N. Clifford, S. A. Haque, T. Lutz and J. R. Durrant, *Chem. Commun.*, 2002, 1464.
31 E. Palomares, J. N. Clifford, S. A. Haque, T. Lutz and J. R. Durrant, *J. Am. Chem. Soc.*, 2003, **125**, 475.
32 J. Jiang, J. A. Spies, J. R. Swierk, A. J. Matula, K. P. Regan, N. Romano, B. J. Brennan, R. H. Crabtree, V. S. Batista, C. A. Schmuttenmaer and G. W. Brudvig, *J. Phys. Chem. C*, 2018, **122**, 13529.
33 B. J. Brennan, M. J. Llansola Portolés, P. A. Liddell, T. A. Moore, A. L. Moore and D. Gust, *Phys. Chem. Chem. Phys.*, 2013, **15**, 16605.
34 J. Jiang, J. R. Swierk, S. Hedström, A. J. Matula, R. H. Crabtree, V. S. Batista, C. A. Schmuttenmaer and G. W. Brudvig, *Phys. Chem. Chem. Phys.*, 2016, **18**, 18678.
35 K. Hanson, M. K. Brennaman, A. Ito, H. Luo, W. Song, K. A. Parker, R. Ghosh, M. R. Norris, C. R. K. Glasson, J. J. Concepcion, R. Lopez and T. J. Meyer, *J. Phys. Chem. C*, 2012, **116**, 14837.
36 M. Liu, S. Makuta, S. Tsuda, S. Russo, S. Seki, J. Terao and Y. Tachibana, *J. Phys. Chem. C*, 2017, **121**, 25672.
37 S. Wang, X. Hai, X. Ding, S. Jin, Y. Xiang, P. Wang, B. Jiang, F. Ichihara, M. Oshikiri, X. Meng, Y. Li, W. Matsuda, J. Ma, S. Seki, X. Wang, H. Huang, Y. Wada, H. Chen and J. Ye, *Nat. Commun.*, 2020, **11**, 1149.
38 S. Ghosh, A. Nakada, M. A. Springer, T. Kawaguchi, K. Suzuki, H. Kaji, I. Baburin, A. Kuc, T. Heine, H. Suzuki, R. Abe and S. Seki, *J. Am. Chem. Soc.*, 2020, **142**, 9752.
39 L. Sun, M. G. Campbell and M. Dincă, *Angew. Chem., Int. Ed.*, 2016, **55**, 3566.
40 M. Ko, L. Mendecki and K. A. Mirica, *Chem. Commun.*, 2018, **54**, 7873.
41 S. K. Bhardwaj, N. Bhardwaj, R. Kaur, J. Mehta, A. L. Sharma, K.-H. Kim and A. Deep, *J. Mater. Chem. A*, 2018, **6**, 14992.
42 T. C. Narayan, T. Miyakai, S. Seki and M. Dincă, *J. Am. Chem. Soc.*, 2012, **134**, 12932.
43 J. Lee, O. K. Farha, J. Roberts, K. A. Scheidt, S. T. Nguyen and J. T. Hupp, *Chem. Soc. Rev.*, 2009, **38**, 1450.
44 M. Rimoldi, A. J. Howarth, M. R. DeStefano, L. Lin, S. Goswami, P. Li, J. T. Hupp and O. K. Farha, *ACS Catal.*, 2017, **7**, 997.
45 D. Yang and B. C. Gates, *ACS Catal.*, 2019, **9**, 1779.
46 K.-i. Otake, J. Ye, M. Mandal, T. Islamoglu, C. T. Buru, J. T. Hupp, M. Delferro, D. G. Truhlar, C. J. Cramer and O. K. Farha, *ACS Catal.*, 2019, **9**, 5383.
47 H. Furukawa, K. E. Cordova, M. O'Keeffe and O. M. Yaghi, *Science*, 2013, **341**, 1230444.

48 J. Gascon, A. Corma, F. Kapteijn and F. X. Llabrés i Xamena, *ACS Catal.*, 2014, **4**, 361.
49 M. Liu, J. Wu and H. Hou, *Chem.–Eur. J.*, 2019, **25**, 2935.
50 A. Dhakshinamoorthy, Z. Li and H. Garcia, *Chem. Soc. Rev.*, 2018, **47**, 8134.
51 G. Lan, Y.-Y. Zhu, S. S. Veroneau, Z. Xu, D. Micheroni and W. Lin, *J. Am. Chem. Soc.*, 2018, **140**, 5326.
52 X. Zhao, B. Pattengale, D. Fan, Z. Zou, Y. Zhao, J. Du, J. Huang and C. Xu, *ACS Energy Lett.*, 2018, **3**, 2520.
53 S. Yang, B. Pattengale, S. Lee and J. Huang, *ACS Energy Lett.*, 2018, **3**, 532.
54 B. Pattengale, J. Neu, S. Ostresh, G. Hu, J. A. Spies, R. Okabe, G. W. Brudvig and C. A. Schmuttenmaer, *J. Am. Chem. Soc.*, 2019, **141**, 9793.
55 J. P. McEvoy and G. W. Brudvig, *Chem. Rev.*, 2006, **106**, 4455.
56 C. Y. Lee, O. K. Farha, B. J. Hong, A. A. Sarjeant, S. T. Nguyen and J. T. Hupp, *J. Am. Chem. Soc.*, 2011, **133**, 15858.
57 J. Zhu, W. A. Maza and A. J. Morris, *J. Photochem. Photobiol., A*, 2017, **344**, 64.
58 W. A. Maza, A. J. Haring, S. R. Ahrenholtz, C. C. Epley, S. Y. Lin and A. J. Morris, *Chem. Sci.*, 2016, **7**, 719.
59 S. R. Ahrenholtz, C. C. Epley and A. J. Morris, *J. Am. Chem. Soc.*, 2014, **136**, 2464.
60 M. Cai, Q. Loague and A. J. Morris, *J. Phys. Chem. Lett.*, 2020, **11**, 702.
61 S. S. Park, E. R. Hontz, L. Sun, C. H. Hendon, A. Walsh, T. Van Voorhis and M. Dincă, *J. Am. Chem. Soc.*, 2015, **137**, 1774.
62 B. Ravel and M. Newville, *J. Synchrotron Radiat.*, 2005, **12**, 537.
63 F. Wudl, G. M. Smith and E. J. Hufnagel, *J. Chem. Soc. D*, 1970, 1453.
64 L. Huchet, S. Akoudad, E. Levillain, J. Roncali, A. Emge and P. Bäuerle, *J. Phys. Chem. B*, 1998, **102**, 7776.
65 F. B. Kaufman, A. H. Schroeder, E. M. Engler, S. R. Kramer and J. Q. Chambers, *J. Am. Chem. Soc.*, 1980, **102**, 483.
66 Y. Mitamura, H. Yorimitsu, K. Oshima and A. Osuka, *Chem. Sci.*, 2011, **2**, 2017.
67 G. Inzelt, J. Q. Chambers and F. B. Kaufman, *J. Electroanal. Chem. Interfacial Electrochem.*, 1983, **159**, 443.
68 T. Amemiya, *J. Electrochem. Soc.*, 1991, **138**, 2845.
69 K. Jackowska, A. Kudelski and J. Bukowska, *Electrochim. Acta*, 1994, **39**, 1365.
70 S. Miertuš, E. Scrocco and J. Tomasi, *Chem. Phys.*, 1981, **55**, 117.
71 M. C. Beard, G. M. Turner and C. A. Schmuttenmaer, *Phys. Rev. B: Condens. Matter Mater. Phys.*, 2000, **62**, 15764.
72 K. P. Regan, J. R. Swierk, J. Neu and C. A. Schmuttenmaer, *J. Phys. Chem. C*, 2017, **121**, 15949.
73 J. B. Baxter and C. A. Schmuttenmaer, *J. Phys. Chem. B*, 2006, **110**, 25229.
74 E. Hendry, M. Koeberg, B. O'Regan and M. Bonn, *Nano Lett.*, 2006, **6**, 755.
75 P. Tiwana, P. Parkinson, M. B. Johnston, H. J. Snaith and L. M. Herz, *J. Phys. Chem. C*, 2010, **114**, 1365.